ELSEVIER

International Journal of Heat and Fluid Flow 20 (1999) 290–301

International Journal of HEAT AND FLUID FLOW

www.elsevier.com/locate/ijhff

Dissimilarity between heat transfer and momentum transfer in a disturbed turbulent boundary layer with insertion of a rod – modeling and numerical simulation

K. Inaoka *, J. Yamamoto, K. Suzuki

Department of Mechanical Engineering, Kyoto University, Kyoto 606-8501, Japan

Abstract

Numerical computation was carried out for a turbulent boundary layer disturbed by a square rod based on a concept of decomposing each quantity into its three components, i.e., time mean, periodical and stochastic fluctuations, respectively. The effect of stochastic fluctuation of velocity and temperature on the time mean and periodically changing parts of flow and thermal fields was modeled with a $k-\varepsilon$ type turbulence model. Numerical results of heat transfer coefficient obtained with a modified LS model agree well with the experimental data. Generation of the dissimilarity between the momentum transfer and heat transfer occurring in the studied boundary layer was successfully predicted. Discussion is developed for the washing action exerted by a spanwise vortex and its role of generating the dissimilarity.

Keywords: Heat transfer; Numerical computation; Dissimilarity; Karman vortex; Three components decomposition

Notation

C_f	skin friction coefficient $=2\tau_w/(\rho u_0^2)$
D	rod size
h	heat transfer coefficient
k	turbulent kinetic energy
Nu	local Nusselt number $=q_w x'/\lambda(\theta_w-\theta_0)$
p	pressure
Pr	Prandtl number
Pr_t	turbulent Prandtl number
q_w	heat flux on the wall
Re_D	rod size based Reynolds number $=Du_0/v$
$Re_{x'}$	streamwise Reynolds number $=x'u_0/v$
u, v	velocities in the x- and y-directions
x, y	streamwise and wall-normal coordinates, see Fig. 2
x'	streamwise location from the leading edge of the flat plate

Greek

δ	thickness of the boundary layer at the origin
ε	dissipation rate of k
v	kinematic viscosity
v_t	turbulent viscosity
λ	thermal conductivity
θ	temperature
ρ	density
τ	shear stress

Subscripts

0	free stream, undisturbed boundary layer
w	wall

Others

$\bar{}$	time mean
$\sim$	periodical part of the fluctuation
$'$	turbulent stochastic component
$\langle\ \rangle$	phase average
$\hat{}$	isotropic

1. Introduction

In a flat plate turbulent boundary layer disturbed by a cylinder mounted normal to the flow direction and detached from the plate, reduction of skin friction of the flat plate was found to appear in the region downstream the inserted cylinder where significant enhancement of heat transfer was observed (Kawaguchi et al., 1984). This opposite direction of change of heat transfer against the one of momentum transfer was called strong dissimilarity (Suzuki and Inaoka, 1998). Later, structural study of turbulence was made near the wall with octant analysis (Suzuki et al., 1988) in the similar disturbed turbulent boundary layer in which the dissimilarity was generated. It was clarified in the study that hot outward and cold wallward interactions were intensified more strongly than sweep and ejection were intensified. Such interactive fluid motions are the motions classified into the first and third quadrants in the u–v

* Corresponding author. E-mail: inaoka@htrans.mech.kyoto-u.ac.jp.

0142-727X/99/$ – see front matter
PII: S0142-727X(99)00015-6

plane where u and v are the streamwise and wall-normal components of velocity fluctuation, respectively. These two interactive fluid motions contribute negatively to momentum transfer. On the other hand, such an intensified wallward interaction was found more likely to be cold, i.e., the one characterized by negative temperature fluctuation, than to be hot. Additionally, the intensified outward interaction is more likely to be hot than to be cold. Therefore, the two types of interactive fluid motions were regarded to contribute positively to heat transfer and result in the generation of the dissimilarity.

Similar larger fractional contribution from the first and third quadrants of the u–v plane were separately reported also for a few types of organized unsteady laminar flows (Suzuki and Suzuki, 1994a; Suzuki and Suzuki, 1994b; Suzuki et al., 1994). In these works, the washing action to be exerted by a spanwise vortex was found to be responsible for the generation of spontaneous dissimilarity which can lead to the dissimilarity between the time mean heat transfer and momentum transfer. Recently, selective intensification of such interactive fluid motions was found to be related to the periodical velocity and temperature fluctuations produced by the Karman vortex in case of a turbulent channel flow obstructed with a square rod (Yao et al., 1995) and in case of a turbulent boundary layer disturbed by a cylinder (de Souza et al., 1997). de Souza et al. (1997) also suggested that the washing action is also important in the generation of the dissimilarity in a disturbed turbulent boundary layer.

The present paper discusses the above topics from an approach different from the previous ones. An effort is made to see if the dissimilarity can be predicted numerically. For this purpose, an unsteady flow numerical computation is carried out for a flat plate turbulent boundary layer disturbed by a square rod by making use of a k–ε type turbulence model. The adopted numerical scheme is developed from the computational code for an unsteady laminar boundary layer disturbed by a square rod (Inaoka et al., 1998), and the periodical shedding of the Karman vortex from the inserted square rod is computed one by one along the time axis. The discussion is developed on the results to be obtained and attention is paid to the roles of the Karman vortex and the washing action exerted by a vortex appearing near the wall.

2. Features of dissimilarity and flow geometry to be studied

As discussed in Section 1, skin friction coefficient C_f and heat transfer coefficient h as well as turbulence quantities have been measured intensively in a turbulent boundary layer disturbed by a cylinder (Suzuki et al., 1988; Suzuki et al., 1991). Typical results on C_f and h are cited from Suzuki et al. (1991) in Fig. 1. Recently, similar experiments were done for the case where a square rod was inserted into a turbulent boundary layer (Inaoka et al., 1997). A square rod was chosen so as to make the geometry of an inserted body more convenient to attach a splitter plate and see if its attachment is effective to suppress the Karman vortex, and therefore, to suppress the dissimilarity. From a grid allocation point of view in a numerical computation, a square rod is preferable as a body to be inserted in the turbulent boundary layer. Therefore, the present numerical computation was made for this geometry shown in Fig. 2. Experimental apparatus and results to be compared with the present numerical computation will be briefly described in the following. Some features of the dissimilarity to be discussed later are also demonstrated here.

Fig. 3 illustrates a low speed wind tunnel used in the experiments (Inaoka et al., 1997). A flat plate 9 was located at the bottom of the wind tunnel of the cross section of 380 mm × 380 mm. Uniformity of free stream velocity was secured at the

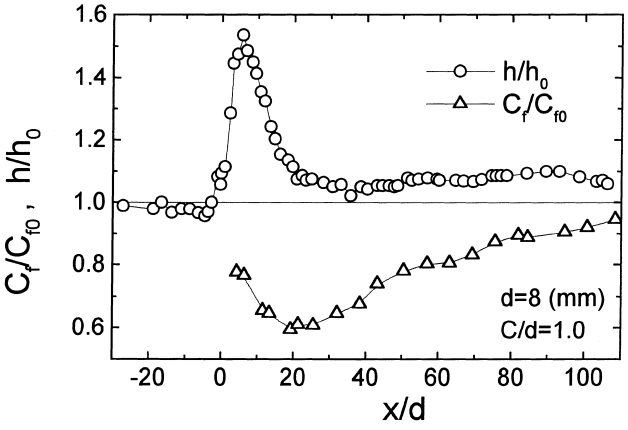

Fig. 1. Distributions of C_f and h/h_0 in a turbulent boundary layer disturbed by a cylinder (Suzuki et al., 1991).

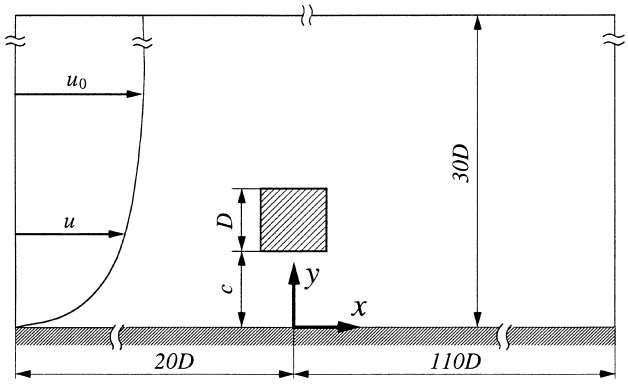

Fig. 2. Computational domain and coordinate system.

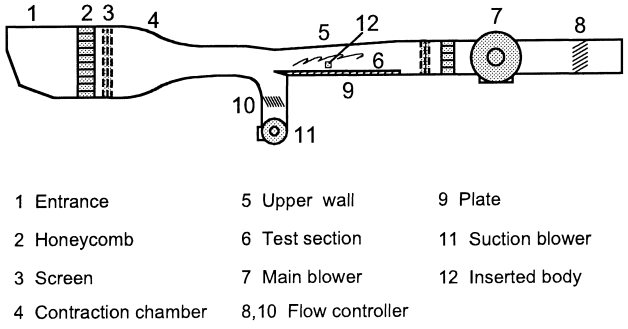

Fig. 3. Schematic view of the wind tunnel.

leading edge of the flat plate by sucking the boundary layer developed on the upstream part of the tunnel floor with a blower 11. The free stream velocity was kept at 14 m/s and streamwise uniformity of static pressure was established by adjusting the geometrical position of the tunnel ceiling. As is shown in Fig. 4, a square rod of 8 mm thickness was mounted at a streamwise position of 1400 mm downstream from the flat plate leading edge in a manner keeping the space between the rod and the flat plate at 8 mm. The thickness of the approaching boundary layer was measured to be 28 mm at the insertion station of the square rod unless it was inserted. The

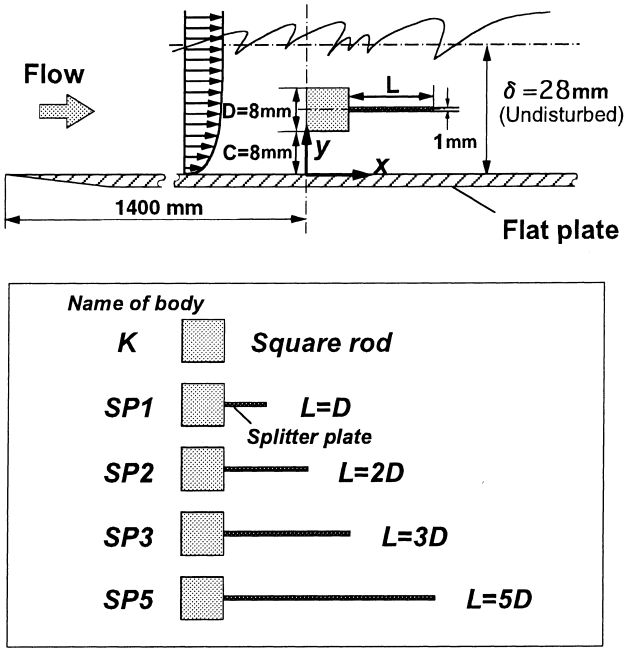

Fig. 4. Geometry of the flow system, coordinate system and geometric parameters (Inaoka et al., 1997).

square rod was positioned parallel to the flat plate and normal to the free stream. Therefore, the studied flow is statistically two-dimensional. In some experiments, a splitter plate of different length was attached to the square rod.

Fig. 5(a) and (b) illustrate the streamwise distributions of the measured heat transfer coefficient and skin friction coefficient, respectively (Inaoka et al., 1997). h_0 in the figure indicates the value of the heat transfer coefficient for a normal flat plate boundary layer without insertion of any disturbing body. It is clearly observed that heat transfer is enhanced by the insertion of the square rod (case K). The results of the present numerical computation are compared in the following with the experimental results of this case K.

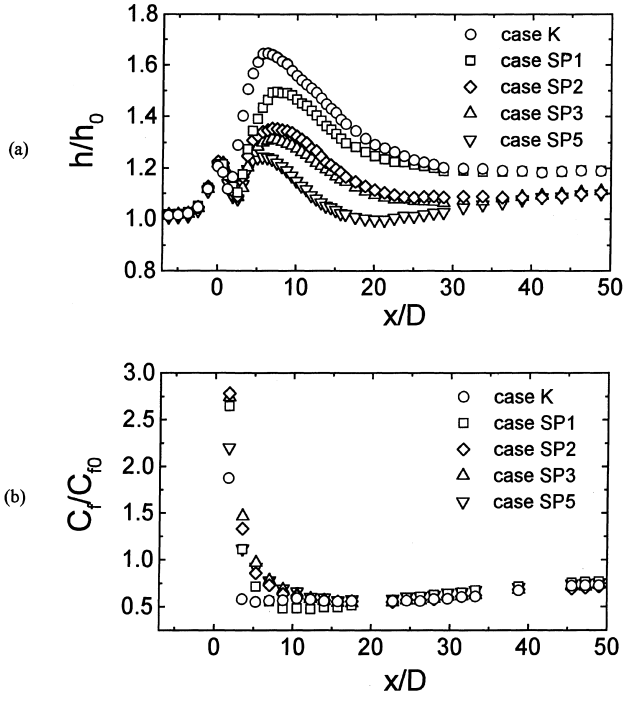

Fig. 5. Streamwise distributions of h/h_0, (a) and C_f/C_{f_0} (b) (Inaoka et al., 1997).

As is seen in Fig. 5(a) and (b), it is observed that enhancement of heat transfer becomes less pronounced with the elongation of the splitter plate. In contrast to this, skin friction coefficient does not change noticeably with the change of the splitter plate length. Fig. 6 shows the power spectra for streamwise component of velocity fluctuation for several cases of different length of the splitter plate (Inaoka et al., 1997). The spectra were measured at a wall-normal position near the flat plate and at the streamwise location near the square rod. Peak of the spectrum becomes less remarkable with the elongation of the splitter plate. Especially, no peak is observable in the spectrum for the case of the longest splitter plate. In this case, heat transfer is least enhanced. Therefore, the Karman vortex or its accompanying periodical fluctuation is concluded to play an important role in generating the dissimilarity. In this sense, three-component decomposition of a quantity, namely decomposition into time mean value, periodical part and stochastic part of fluctuation, is needed in the numerical computation to successfully predict the generation of dissimilarity. This necessity was also pointed out by Yao et al. (1995) in their paper on a turbulent channel flow disturbed by an inserted square rod.

In the experiments on a turbulent boundary layer disturbed by a cylinder, de Souza et al. (1997) showed that the Karman vortex shed from the lower half of the inserted body disappears in a short distance and that another vortex shed from the upper half keeps a much longer life. It was also observed in their experiments that the latter vortex approaches to the flat plate and that it exerts a washing action to the flat plate surface. This washing action was confirmed to be the generation mechanism of the dissimilarity, as was concluded by Suzuki et al. (Suzuki and Suzuki, 1994a; Suzuki and Suzuki, 1994b) in a series of numerical studies of an unsteady channel flow partially blocked with a square rod.

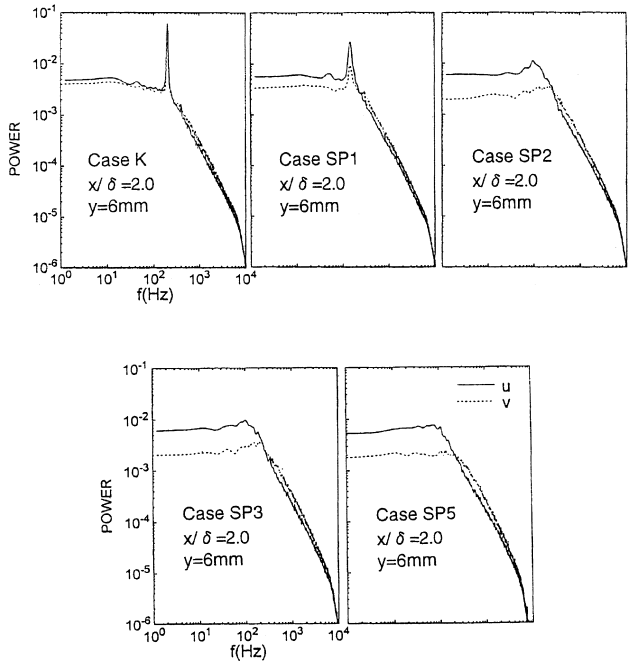

Fig. 6. Power spectrum of u and v (Inaoka et al., 1997).

3. Computational method and procedures

The following three components decomposition is adopted for a velocity component in x_i direction, u_i, pressure p and temperature θ:

$$u_i = \bar{u}_i + \tilde{u}_i + u_i' = \langle u_i \rangle + u_i', \tag{1}$$

$$p = \bar{p} + \tilde{p} + p' = \langle p \rangle + p', \tag{2}$$

$$\theta = \bar{\theta} + \tilde{\theta} + \theta' = \langle \theta \rangle + \theta', \tag{3}$$

where $\overline{A}$ denotes the time mean value of a quantity A, $\tilde{A}$ designates the periodical part of the fluctuation of the quantity and A' the turbulent stochastic component of the fluctuation of the quantity. $\langle\ \rangle$ denotes the phase average.

The governing equations for u_i may be written as follows:

$$\frac{\partial u_i}{\partial x_i} = 0, \tag{4}$$

$$\frac{\partial u_i}{\partial t} + u_j \frac{\partial u_i}{\partial x_j} = -\frac{\partial p}{\partial x_i} + \frac{1}{\mathrm{Re}} \frac{\partial^2 u_i}{\partial x_j \partial x_j}, \tag{5}$$

where t is time and Re is the flow Reynolds number.

Substituting Eqs. (1)–(3) into Eq. (5), taking into account of Eq. (4) and then phase averaging, one obtains the following equation for $\langle u_i \rangle$ (Reynolds and Hussain, 1972):

$$\frac{\partial \langle u_i \rangle}{\partial t} + \langle u_i \rangle \frac{\partial \langle u_i \rangle}{\partial x_j} = -\frac{\partial \langle p \rangle}{\partial x_i} + \frac{1}{\mathrm{Re}} \frac{\partial^2 \langle u_i \rangle}{\partial x_j \partial x_j} - \frac{\partial}{\partial x_j} \langle u_i' u_j' \rangle. \tag{6}$$

The third term of the right-hand side of Eq. (6) is modeled with a turbulence model as was made in the other references (Cousteix et al., 1978; Ha Minh et al., 1989; MacInnes et al., 1989; Franke and Rodi, 1991; Kato and Launder, 1993; Bosch and Rodi, 1996). Here is used a low Reynolds number version of the $k-\varepsilon$ turbulence model, i.e., Launder and Sharma, 1974 model hereafter referred as LS model) but with a little modification so as to describe the stochastic parts of velocity field on the phase averaged velocity field, namely:

$$-\left\langle u_i' u_j' \right\rangle = \nu_t \left(\frac{\partial \langle u_i \rangle}{\partial x_j} + \frac{\partial \langle u_j \rangle}{\partial x_i} \right) - \frac{2}{3} \delta_{ij} \langle k \rangle, \tag{7}$$

where

$$\nu_t = C_\mu f_\mu \frac{\langle k \rangle^2}{\langle \hat{\varepsilon} \rangle}, \quad C_\mu = 0.09, \quad f_\mu = \exp\left\{ \frac{-3.4}{(1 + R_t/50)^2} \right\},$$
$$R_t = \frac{\langle k \rangle^2}{\nu \langle \hat{\varepsilon} \rangle}. \tag{8}$$

Phase averaged turbulent kinetic energy $\langle k \rangle$ and the rate of its dissipation $\langle \varepsilon \rangle$ are determined from the following transport equations in the case where the LS model is employed:

$$\frac{\partial \langle k \rangle}{\partial t} + \langle u_j \rangle \frac{\partial \langle k \rangle}{\partial x_j} = \frac{\partial}{\partial x_j} \left\{ \left(\nu + \frac{\nu_t}{\sigma_k} \right) \frac{\partial \langle k \rangle}{\partial x_j} \right\} + P_k - (\langle \hat{\varepsilon} \rangle + D), \tag{9}$$

$$\frac{\partial \langle \hat{\varepsilon} \rangle}{\partial t} + \langle u_j \rangle \frac{\partial \langle \hat{\varepsilon} \rangle}{\partial x_j} = \frac{\partial}{\partial x_j} \left\{ \left(\nu + \frac{\nu_t}{\sigma_\varepsilon} \right) \frac{\partial \langle \hat{\varepsilon} \rangle}{\partial x_j} \right\} + C_{\varepsilon 1} f_1 \frac{\langle \hat{\varepsilon} \rangle}{\langle k \rangle} P_k - C_{\varepsilon 2} f_2 \frac{\langle \hat{\varepsilon} \rangle^2}{\langle k \rangle} + E, \tag{10}$$

where

$$P_k = \nu_t S^2, \quad S = \sqrt{\frac{1}{2} \left(\frac{\partial \langle u_i \rangle}{\partial x_j} + \frac{\partial \langle u_j \rangle}{\partial x_i} \right)^2}, \quad D = 2\nu \left(\frac{\partial \sqrt{\langle k \rangle}}{\partial x_j} \right)^2,$$
$$\langle \hat{\varepsilon} \rangle = \langle \varepsilon \rangle - D, \quad E = 2\nu\mu_t \left(\frac{\partial^2 \langle u_i \rangle}{\partial x_j \partial x_i} \right)^2, \quad f_1 = 1.0,$$
$$f_2 = 1.0 - 0.3 \exp\left(-R_t^2 \right), \tag{11}$$
$$C_{\varepsilon 1} = 1.14, \quad C_{\varepsilon 2} = 1.92, \quad \sigma_k = 1.0, \quad \sigma_\varepsilon = 1.3.$$

$\hat{\varepsilon}$ is the isotropic part of the dissipation rate. Adoption of $\hat{\varepsilon}$ as a variable simplifies the wall boundary condition of the dissipation rate since $\hat{\varepsilon} = 0$ at the wall.

In order to reduce the excessive production of $\langle k \rangle$ predicted in the stagnation regions with LS model, Kato–Launder model (1993, hereafter referred as KL model) proposed to replace the production expression P_k by

$$P_k = \nu_t S \Omega, \quad \Omega = \sqrt{\frac{1}{2} \left(\frac{\partial \langle u_i \rangle}{\partial x_j} - \frac{\partial \langle u_j \rangle}{\partial x_i} \right)^2} \tag{12}$$

was also tested in the present study.

Similarly, energy equation can be expressed with $\langle \theta \rangle$ as follows:

$$\frac{\partial \langle \theta \rangle}{\partial t} + \langle u_j \rangle \frac{\partial \langle \theta \rangle}{\partial x_j} = \frac{1}{\mathrm{Re\,Pr}} \frac{\partial^2 \langle \theta \rangle}{\partial x_j \partial x_j} - \frac{\partial \langle u_i' \theta' \rangle}{\partial x_j}, \tag{13}$$

$$-\left\langle u_i' \theta' \right\rangle = \frac{\nu_t}{\mathrm{Pr}_t} \frac{\partial \langle \theta \rangle}{\partial x_i}. \tag{14}$$

Unsteady flow Prandtl number was assumed to be constant in this study, namely $\mathrm{Pr}_t = 0.9$.

Fully implicit forms of finite difference equivalents of the above mentioned equations were solved numerically along the time axis. For the finite-differencing of the governing equations, a central finite-differencing scheme was used for the diffusion terms. For the convection terms, the third-order upwind scheme (QUICK) was applied in case of the momentum equation but the central finite-differencing scheme in cases of the $\langle k \rangle$, $\langle \hat{\varepsilon} \rangle$ and energy equations. For the evaluation of pressure, the SIMPLE algorithm was employed. In order to relax the solutions of the above types of elliptic differential equations, iterative process was applied at each time step. In this process, alternating direction implicit (ADI) method was also combined.

The geometry treated in the present study is illustrated in Fig. 2, together with the coordinate system to be used below. A square rod is mounted in a flat plate turbulent boundary layer in a position normal to the flow direction and detached from the flat plate. The conditions for which computation is made are shown in Table 1. In the present study, main stream velocity u_0 ($= 14$ m/s) was treated constant and the square rod of the size D ($= 8$ mm) was introduced at the location of streamwise Reynolds number $\mathrm{Re}_{x'} = 1.24 \times 10^6$. The inlet and outlet boundaries of the computational domain were located at $20D$ upstream and $110D$ downstream from the square rod

Table 1
Conditions for computation

u_0	14.0 m/s
D	8 mm
Re_D	7075
$\mathrm{Re}_{x'}$	1.24×10^6
δ_0	25 mm
c/D	1.0

position, respectively. The free stream boundary was located at $y = 30D$. 200×110 grid points were allocated non-uniformly in the computational domain with fine grid meshes near the flat plate and the square rod. Especially, more than two grid points were allocated within the viscous sublayer in order to evaluate quantities near the flat plate accurately. The upstream boundary condition for the streamwise velocity $\langle u \rangle$ was given as follows:

$$u^+ = y^+ \quad (y^+ \leqslant 5)$$
$$u^+ = 5.0 + 5.0 \ln(y^+/5.0) \quad (5 < y^+ \leqslant 30)$$
$$u^+ = 2.44 \ln y^+ + 5.0 + 2.44\Pi W(y/\delta) \qquad (30 < y^+) \tag{15}$$

where

$$W(y/\delta) = 2 \sin^2(\pi y/2\delta), \quad \Pi = 0.596,$$
$$y^+ = \frac{u^* y}{\nu}, \quad u^+ = \frac{u}{u^*}. \tag{16}$$

In order to determine other quantities such as $\langle v \rangle$, $\langle k \rangle$, $\langle \hat{\varepsilon} \rangle$ and $\langle \theta \rangle$ at the upstream boundary, preliminary steady numerical computation was made for a normal undisturbed flat plate turbulent boundary layer in the smaller region of $-30 \leqslant x/D \leqslant -17.5$. As the upstream boundary condition for that preliminary calculation, $\langle v \rangle$ was assumed to be zero, $\langle k \rangle$ and $\langle \hat{\varepsilon} \rangle$ were given by the DNS results (Mansour et al., 1988), and $\langle \theta \rangle$ was given by the experimental data obtained by the above mentioned wind tunnel. The results obtained at $x/D = 20$ were adopted as the upstream boundary condition in the main computation.

At the downstream boundary, streamwise gradients of all quantities were assumed to be 0. At the free stream boundary, the streamwise velocity and the cross-stream velocity were set to be u_0 ($= 14$ m/s) and 0, respectively. The cross-stream gradients of the other quantities were set to be 0. At the solid boundary, no-slip condition was used. The square rod surfaces were treated to be thermally insulated and uniform heat flux was assumed at the flat plate surface.

The above set of equations was numerically solved and the time mean Nusselt number and time mean skin friction coefficient were calculated. The obtained results will be compared with the experimental data discussed in the above.

4. Numerical results and discussions

Here are discussed the obtained numerical results in comparison with the experimental data. Fig. 7(a) shows the streamwise distributions of time mean Nusselt number $\overline{\mathrm{Nu}}$ and Fig. 7(b) those of time mean skin friction coefficient $\overline{C_\mathrm{f}}$. In these figures, both values are normalized with the respective counterparts of the undisturbed boundary layer. It is observed in Fig. 7(a) that the present computed distribution of the time mean Nusselt number with LS model is quite similar in shape as the experimental data obtained by Inaoka et al. (1997) while the enhancement of heat transfer is calculated in a little less pronounced manner. Skin friction coefficient calculated with LS model also closely follows the experimental values obtained by Inaoka et al. (1997). The reduction of skin friction is predicted in a little less pronounced manner. Thus, the dissimilarity is predicted a little weakly. In particular, increase of heat transfer coefficient accompanying the reduction of skin friction, which we call strong dissimilarity, is obtained only at positions downstream the position of $x/D = 9$, in contrast to the experimental result that it is achieved at positions downstream the location of $x/D = 2$. In that sense, further improvement of the model is still requested; however, an important point is that the generation of strong dissimilarity was predicted first time and was possible only through the present type of unsteady flow computation based on the three-component decomposition approach. Such success has never been achieved with steady flow computations employing a few different turbulence models in attempts by the group of the present author. Although the results of the skin friction coefficient obtained with KL model agree with the experimental data better than those with LS model, unreasonable results were observed in the Nusselt number distribution. Thus, the discussion will be concentrated in the following on the generation mechanism of the dissimilarity based on the results obtained with the LS model.

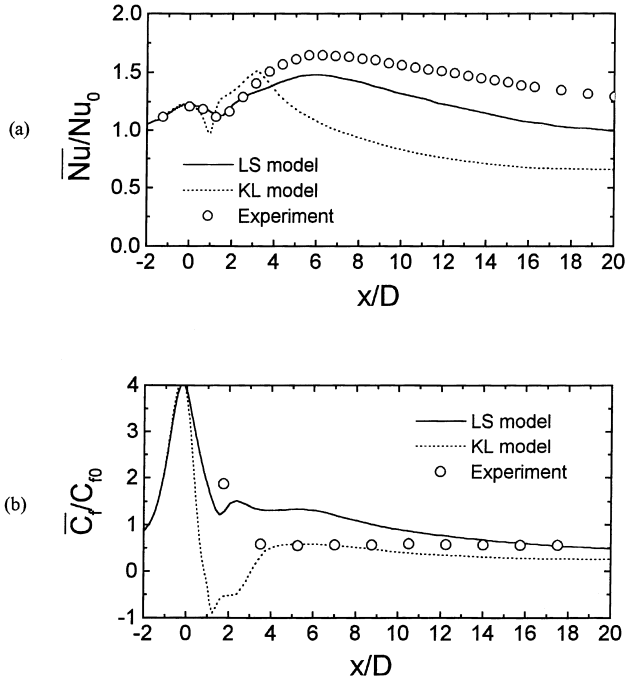

Fig. 7. Streamwise distributions of time mean Nusselt number (a) and skin friction coefficient (b).

As will be mentioned later, flow and thermal fields change in a highly periodic manner accompanied by a Karman-like vortex shed from the square rod. Therefore, in order to investigate the instantaneous flow and thermal field structures, several quantities were sampled at each instant corresponding to every one eighth of a period of the velocity fluctuation. Fig. 8(a) and (b) show the streamwise distributions of the instantaneous Nusselt number Nu and those of the instantaneous skin friction coefficient C_f sampled that way, respectively. In each frame of these figures, instantaneous distributions of Nusselt number and skin friction coefficient are presented with solid lines together with their time mean values, $\overline{\mathrm{Nu}}$ and $\overline{C_\mathrm{f}}$, illustrated by dotted lines. Time change of Nu and C_f distributions are clearly observed in these figures. Similar to the distribution of $\overline{\mathrm{Nu}}$, the distribution of Nu has two or three peaks at every instant. While its first peak constantly appears at a position close to the square rod, its second peak changes its position from one sampling phase to another, i.e., the second peak position moves downstream with an elapse of time. The same feature of time variation is clearly observed in the distribution of C_f. In these figures one interesting feature can be observed. Namely, peak instantaneous heat transfer coefficient is generated at positions where the dent is observed in the distribution of instantaneous skin friction coefficient. This means that instantaneous dissimilarity between heat transfer and momentum transfer is locally generated there. The positions where such instantaneous

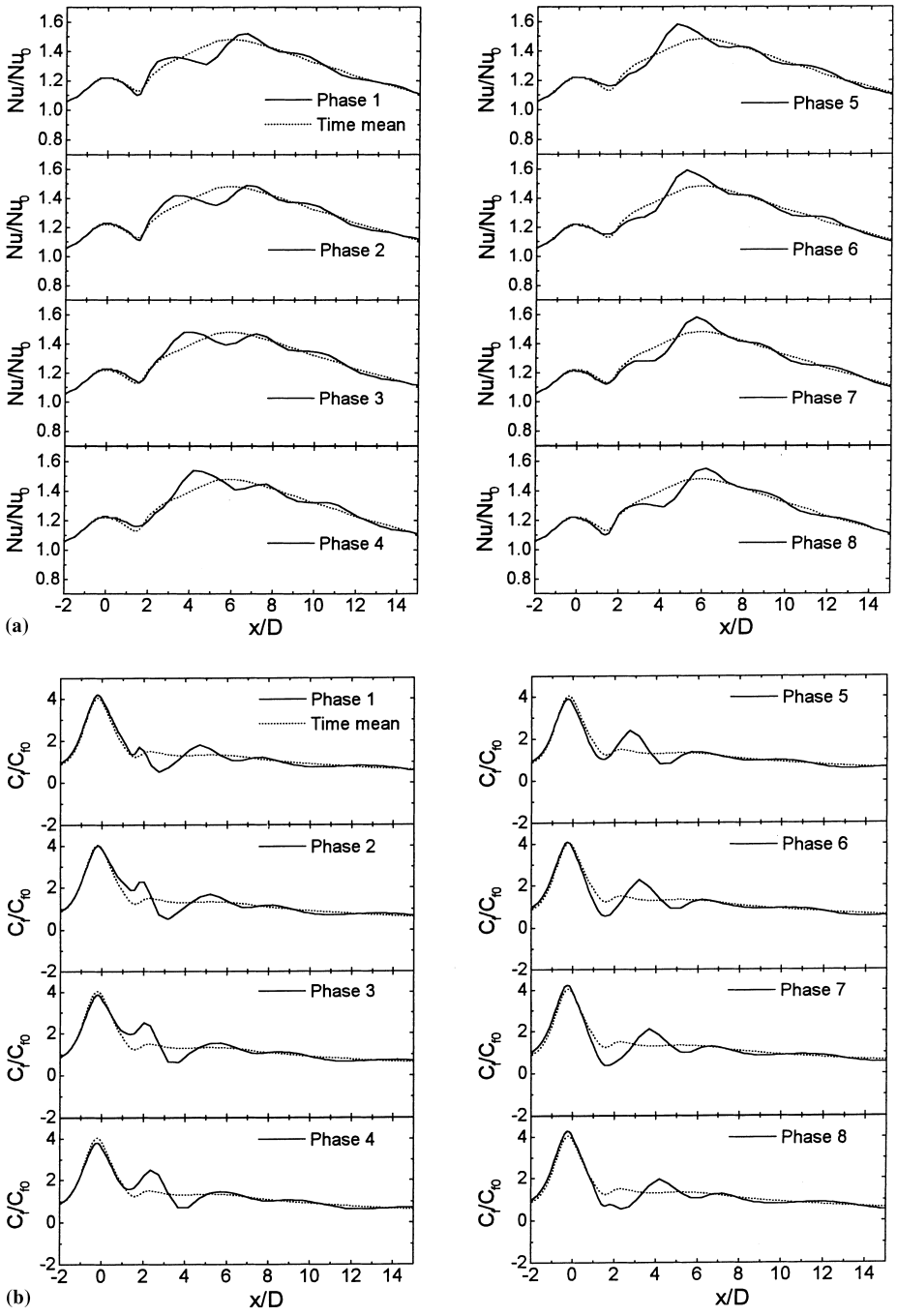

Fig. 8. (a) Streamwise distributions of instantaneous Nusselt number. (b) Streamwise distributions of instantaneous skin friction coefficient.

dissimilarity appears move downstream with an elapse of time. Such a local instantaneous dissimilarity observed at every instant contributes to the generation of the time mean dissimilarity found in Fig. 7(a) and (b).

Fig. 9 compares the spatial distributions of an instantaneous apparent wall-normal heat flux produced by the periodical fluctuations of velocity and temperature, $\tilde{v}\tilde{\theta}$, and another instantaneous apparent heat flux produced by the stochastic fluctuations of velocity and temperature, $\langle v'\theta'\rangle$, sampled at several instants. $\tilde{v}\tilde{\theta}$ is calculated automatically as a part of convection term of Eq. (13) while $\langle v'\theta'\rangle$ is calculated through the model of Eq. (14) in the present computation. In this figure, the shaded parts correspond to the regions where the plotted quantities take positive value, namely heat is transferred outwards in the boundary layer and the unshaded parts to those where they take negative value. Deep gray colored area corresponds to the large heat flux region. The arrow in the figure represents the peak position of instantaneous Nusselt number or the position where the dissimilarity exists. Since the shaded area covers almost all parts of the boundary layer both for $\tilde{v}\tilde{\theta}$ and $\langle v'\theta'\rangle$, both of periodical and stochastic fluctuations enhance the heat transfer inside the boundary layer. This should lead to the enhancement of the time mean wall heat transfer. At the bottom of this figure, bird's-eye view presentations of instantaneous distributions of $\tilde{v}\tilde{\theta}$ and $\langle v'\theta'\rangle$ sampled at a particular instant are plotted. Another point

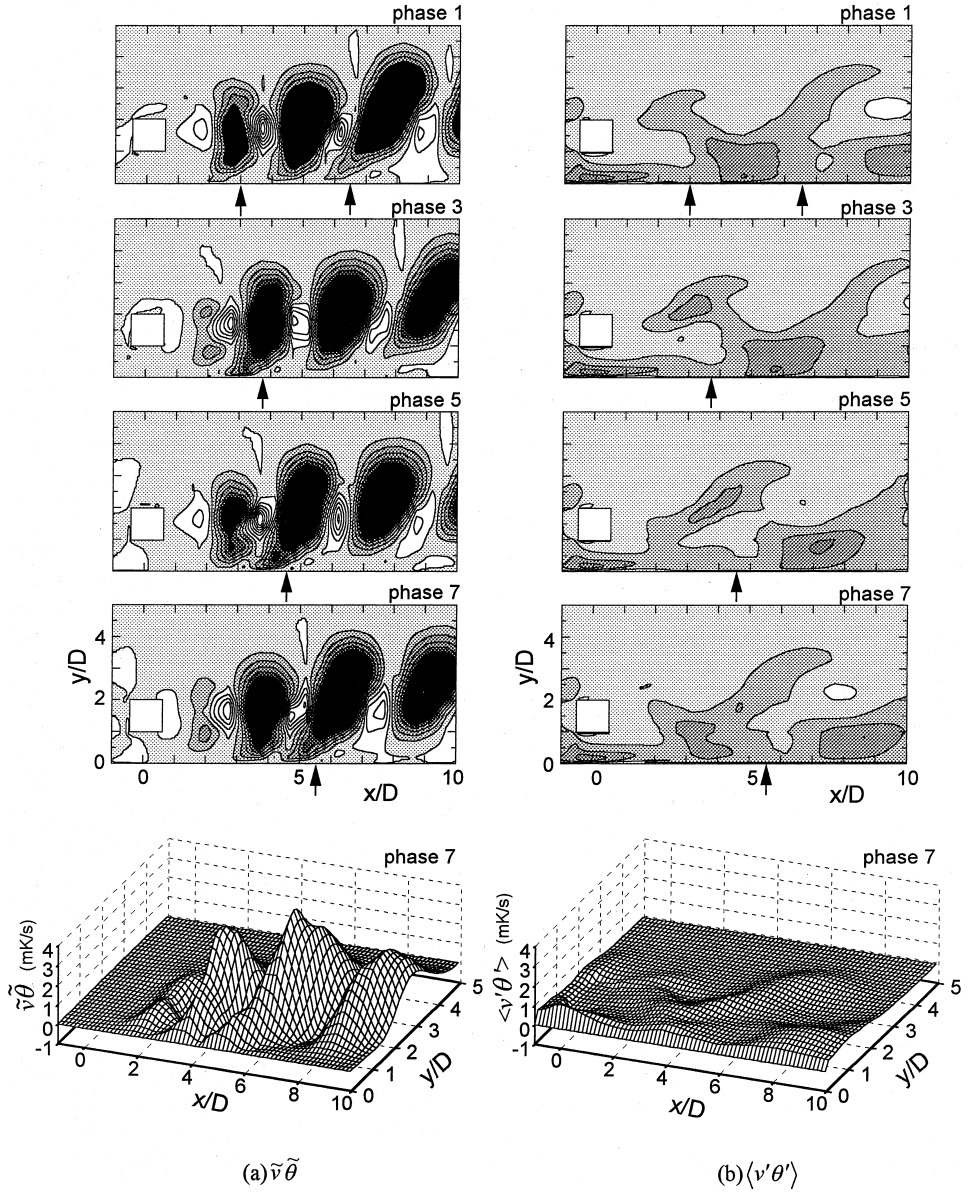

Fig. 9. Instantaneous maps of heat flux contours: (a) $\tilde{v}\tilde{\theta}$ and (b) $\langle v'\theta'\rangle$ (shaded parts: positive value).

worthy to notice is that $\tilde{v}\tilde{\theta}$ takes much larger value than $\langle v'\theta'\rangle$ inside the boundary layer and that such larger value of $\tilde{v}\tilde{\theta}$ appears just above the peak position of Nu indicated by the arrow at each instant. Therefore, the periodical part of fluctuations should contribute majorly to the production of peak Nu and therefore the enhancement of the time mean wall heat transfer.

Fig. 10 compares the spatial distributions of an instantaneous apparent wall-normal Reynolds shear stress produced by the periodical velocity fluctuations $-\tilde{u}\tilde{v}$ and another instantaneous apparent Reynolds shear stress produced by the stochastic velocity fluctuations $-\langle u'v'\rangle$ in the same manner as seen in Fig. 9. In this figure, again the shaded parts correspond to the regions where the plotted quantities take positive value and unshaded parts to those take negative value. It is confirmed that not only stochastic fluctuation but also periodical fluctuation produces large value of apparent shear stress inside the boundary layer. As is observed in the experimental data by Inaoka et al. (1997), large negative shear stress is attained in the distribution of $-\tilde{u}\tilde{v}$ near the wall, especially at the position just above the peak position of Nu or the minimum peak position of C_f indicated by the arrow at each instant. This should contribute majorly to the production of minimum peak of C_f and therefore the reduction of the time mean skin friction. Thus, such spatial distributions of the apparent positive heat transfer and apparent negative momentum transfer instantaneously produced near the wall are the direct cause of the dissimilarity in the distributions between Nu and C_f found in Fig. 8. Therefore, taking such large contribution from the periodical component of fluctuations into consideration is crucial in numerical computation to successfully predict the dissimilarity in the studied boundary layer. In the following, detail discussion on the generation mechanism of the dissimilarity will be developed focused on such periodical fluctuations.

Figs. 11 and 12, respectively, show the instantaneous contour maps of the vorticity and temperature, which were sampled at the same instant as the one for each frame of Fig. 8(a)

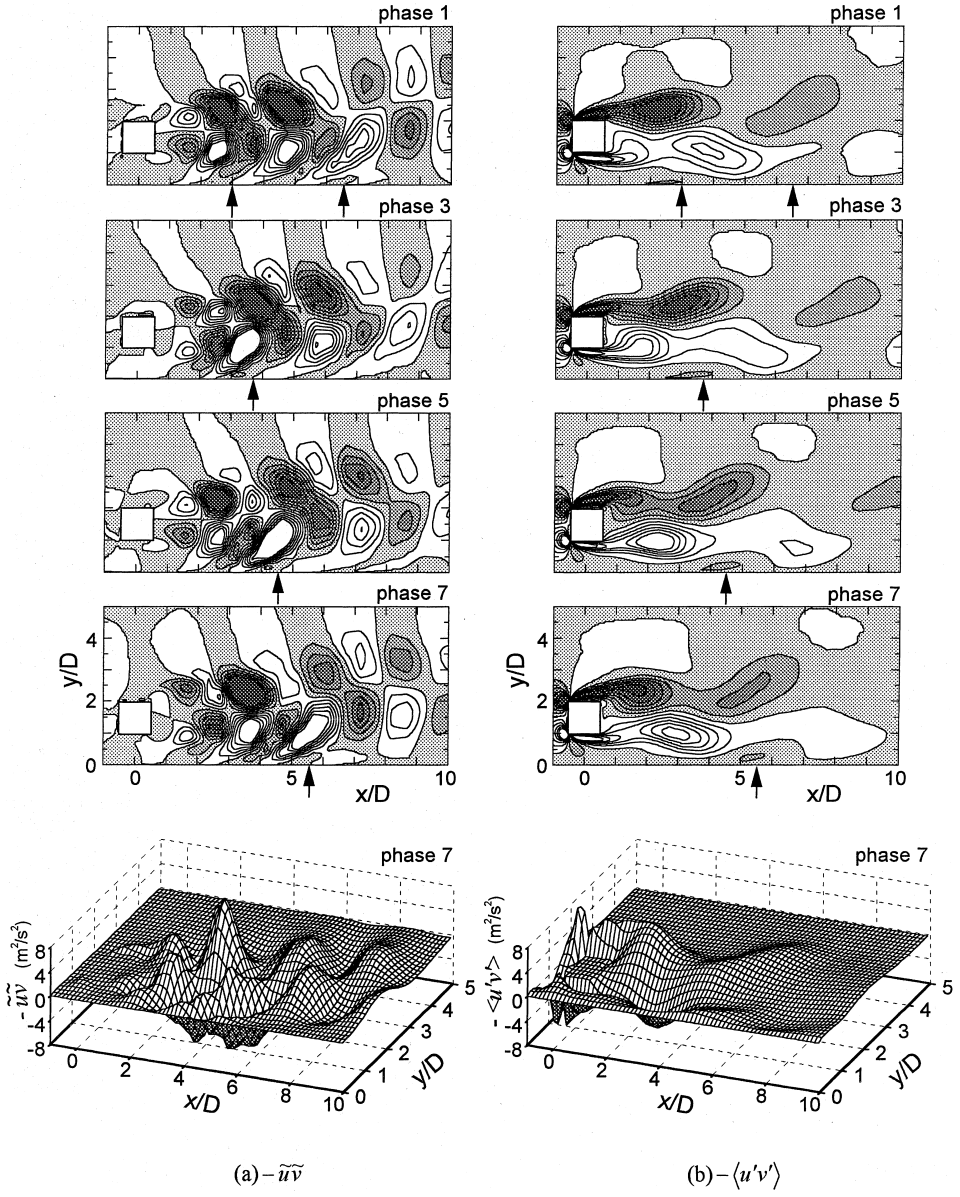

Fig. 10. Instantaneous maps of shear stress contours: (a) $-\tilde{u}\tilde{v}$ and (b) $-\langle u'v'\rangle$ (shaded parts: positive value).

and (b). In Fig. 11, the shaded parts correspond to the regions where vorticity is positive and the unshaded parts to those where it is negative. The arrow in the figure again represents the peak position of instantaneous Nusselt number or the position where the dissimilarity exists. Time dependent behavior of the Karman vortex shed from the square rod can be observed in these figures but it is distorted by the effect of the shear existing in the boundary layer. Negative-vorticity region (hereafter called NS region) which is formed in the upper half of the near wake of the square rod rotates clockwisely as it moves downstream with an elapse of time (phase1 → phase4). Simultaneously, this NS region drives the positive-vorticity region (hereafter called PS region) which is formed in the lower half of the near wake of the square rod upward (phase3 → phase7). As is observed in Fig. 12 the NS region supplies the cooler fluid from the outer region of the boundary layer toward the wall and the PS region ejects the hotter fluid from near-wall region toward the outer region. Both enhance the wall heat transfer.

The above mentioned motions of the PS and NS regions produce another important unsteady flow behavior. High-vorticity wall layer developing near the flat plate surface is intensified in vorticity at the insertion position of the rod due to the flow acceleration occurring in the space between the rod and the flat plate. Fig. 13 shows the magnified view of the instantaneous contour maps of the vorticity near the flat plate, which were sampled at several instants. It is clearly observed that, synchronizely assisted by the motion of the PS and NS regions, the tip of this high-vorticity wall layer (hereafter called NW tongue) protrude outward or is lifted just around the peak Nu position indicated by an arrow. Fig. 14 shows the instantaneous vector map of the periodically fluctuating velocity, $\tilde{u}-\tilde{v}$, together with the instantaneous periodical part of temperature fluctuation, $\tilde{\theta}$. These are sampled at the instants same as those of Fig. 13. In Fig. 14, the shaded parts indicate the region where $\tilde{\theta}$ is positive and unshaded parts the region where it is negative. It is clearly observed in this figure that clockwise fluid motion is induced around the lifted tip of the NW tongue

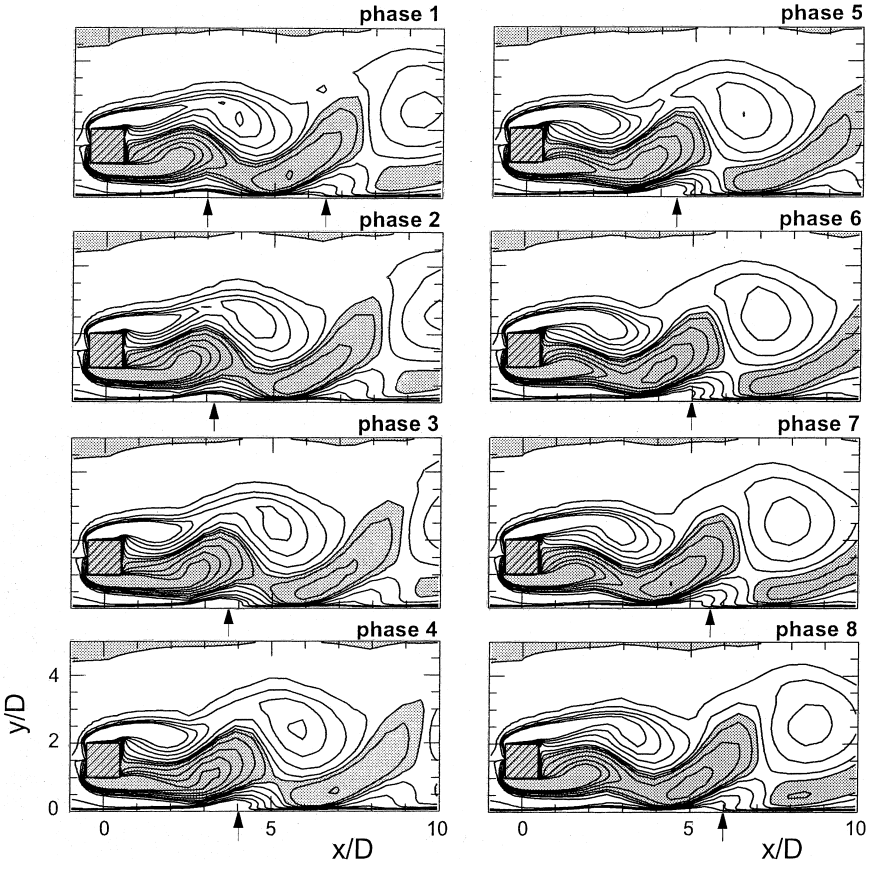

Fig. 11. Instantaneous maps of the vorticity contours (shaded parts: vorticity is positive).

observed in Fig. 13. This clockwise fluid motion entrains fresh and cooler fluid into the near-wall region below the NW tongue from its downstream side so that heat transfer enhancement is achieved there. Since this fluid motion entrains the fluid into the near-wall region from the downstream side, it temporarily reduces the streamwise velocity there near the wall so that skin friction reduction occurs there. At the upstream side of its clockwise fluid motion, appearance of an intense upflow from the near-wall region to the outside is observed. The upflow is effective in pumping out the hotter fluid that has exchanged heat with the wall surface. It prevents from the excess heating of the wall and is thus effective in enhancing the heat transfer, too. Above mentioned clockwise fluid motion is clearly observed to lie just above the peak position of Nu indicated by an arrow, and it is the washing action of a spanwise vortex appearing near the wall discussed for a different type of unsteady flows in Suzuki and Suzuki (1994a); Suzuki and Suzuki (1994b); and Inaoka et al. (1998). This washing action of the vortex appearing near the wall should be the cause of the generation mechanism of the dissimilarity and therefore, precise prediction of the periodical component of fluctuation is again concluded to be decisive to successfully predict the dissimilarity.

On the other hand, such entrainment of cooler fluid and pumping out of the heated fluid caused by the washing action exerted by the vortex are characterized by $\tilde{u} < 0$, $\tilde{v} < 0$ and $\tilde{\theta} < 0$, and $\tilde{u} > 0$, $\tilde{v} > 0$ and $\tilde{\theta} > 0$, respectively. Thus, they are classified into the elementary fluid motions equivalent to the "cold wallward interaction" and "hot outward interaction" of turbulent elementary fluid motions. They contribute negatively to momentum transfer but positively to heat transfer and thus result in generating the dissimilarity. Figs. 15 and 16, respectively, show the magnified view of the spatial distribution of the contours of $-\tilde{u}\tilde{v}$ and $\tilde{v}\tilde{\theta}$. In these figures, the shaded parts indicate the region where the value of the plotted quantity is positive and unshaded parts the region where it is negative. From these figures, such interactive fluid motions are confirmed to be produced in the near-wall region around the position indicated by an arrow. $-\tilde{u}\tilde{v}$ takes negative value but $\tilde{v}\tilde{\theta}$ takes positive value just downstream the positions specified by the arrows. Thus, two types of interactive fluid motions are confirmed to be periodically intensified by the washing action. Therefore, as was suggested by de Souza et al. (1997), selective intensification of such interactive fluid motions observed in a disturbed turbulent flow should be related to the washing action periodically exerted by a vortex near the wall.

5. Concluding remarks

Numerical computation was carried out for a turbulent boundary layer disturbed by a square rod based on a concept of decomposing each quantity into its three components, i.e., time mean, periodical and stochastic ones. The effect of stochastic fluctuation of velocity and temperature on the time mean and periodically changing parts of flow and thermal fields was modeled with a $k-\varepsilon$ type turbulence model.

Obtained results of heat transfer coefficient with LS model agree fairly well with the experimental data. In the results obtained with the LS model, heat transfer enhancement and generation of the dissimilarity between momentum transfer and heat transfer in the studied boundary layer were predicted.

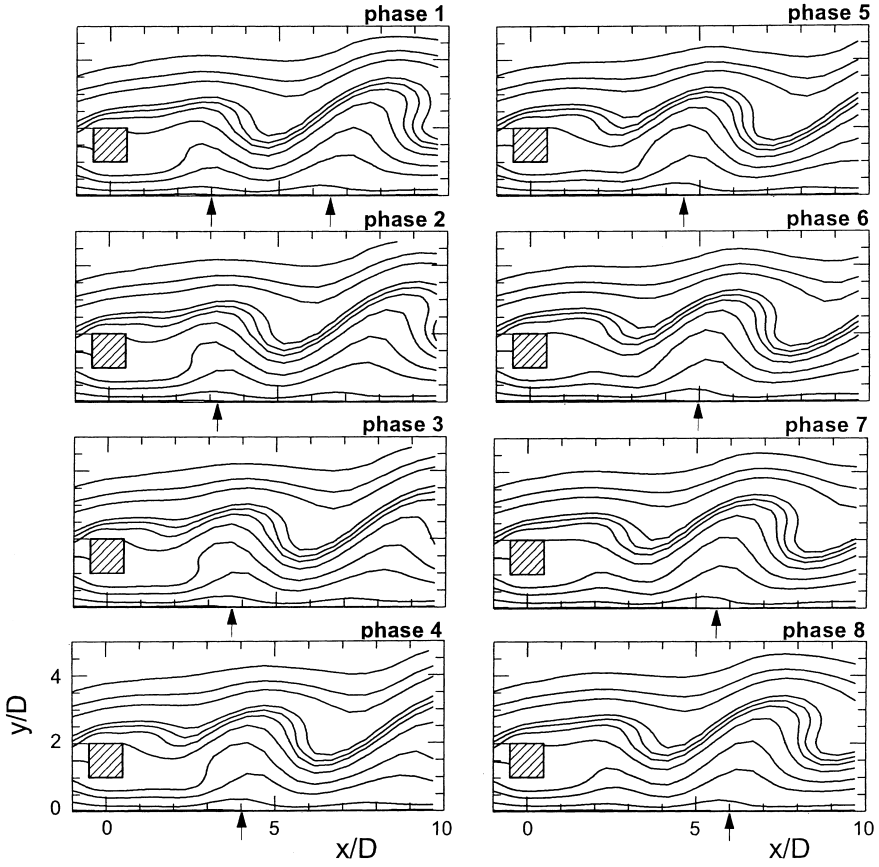

Fig. 12. Instantaneous maps of the temperature contours.

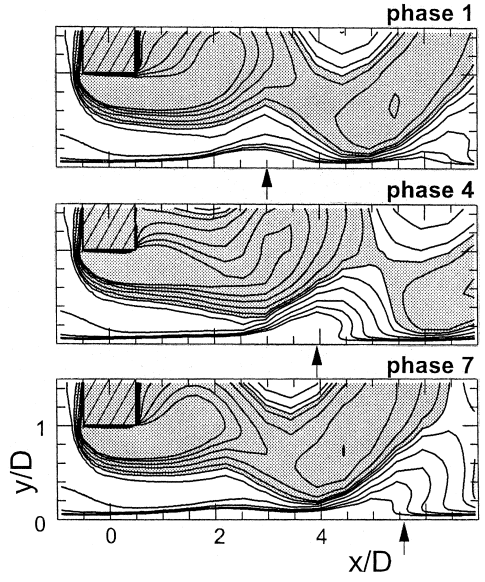

Fig. 13. Instantaneous maps of the vorticity contours, magnified view (shaded parts: vorticity is positive).

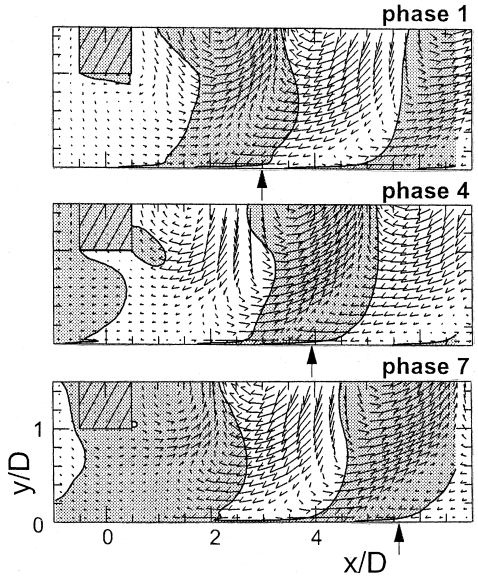

Fig. 14. Instantaneous distribution of the fluctuating velocity vector, $\tilde{u} - \tilde{v}$ (shaded parts: hotter than time mean temperature).

This dissimilarity results from the occurrence of the instantaneous dissimilarity. Generation mechanism of the instantaneous dissimilarity is strongly related to the behavior of the Karman vortex. Namely, taking large contribution from the periodical component of fluctuations into consideration is decisive in numerical computation to predict the dissimilarity. Therefore, three components decomposition of a quality is very necessary in numerically predicting the dissimilarity. A

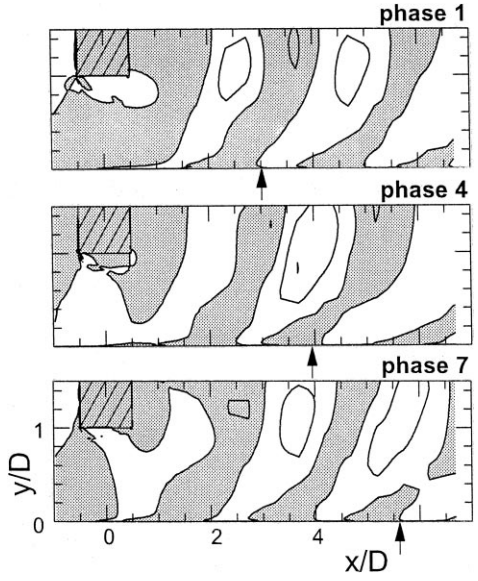

Fig. 15. Instantaneous maps of $-\tilde{u}\tilde{v}$ (shaded parts: the value of $-\tilde{u}\tilde{v}$ is positive).

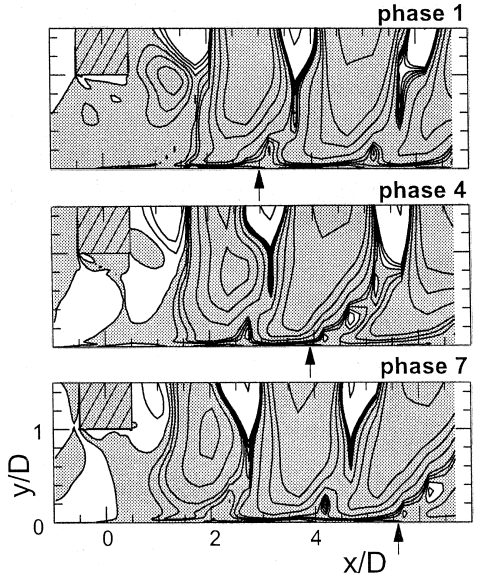

Fig. 16. Instantaneous maps of $\tilde{v}\tilde{\theta}$ (shaded parts: the value of $\tilde{v}\tilde{\theta}$ is positive).

downstream tip of the high-vorticity wall layer lifted from the wall induces a clockwise motion producing the effects called washing action around it. This washing action produces the dissimilarity. Namely, it supplies cooler fresh fluid into the near-wall region from the downstream side and ejects the hotter fluid toward outside from the wall region at the upstream side. This washing action can fairly well explain the experimental results that the selective intensification of two types of interactive fluid motions was observed.

References

Bosch, G., Rodi, W., 1996. Simulation of vortex shedding past a square cylinder near a wall. Proc. 10th Symp. Turbulent Shear Flows, 4-13–4-18.

Cousteix, J., Desopper, A., Houdeville, R., 1978. Structure and development of a turbulent boundary layer in an oscillatory external flow. Turbulent Shear Flows, Springer, Berlin, 154–171.

de Souza, F., Delville, J., Lewalle, J., Bonnet, J.P., 1997. On the large scale organization of a turbulent boundary layer disturbed by a circular cylinder. Proc. 11th Symp. Turbulent Shear Flows, vol. 3, 33.25–33.30.

Franke, R., Rodi, W., 1991. Calculation of vortex shedding past a square cylinder with various turbulence models. Proc. 8th Symp. Turbulent Shear Flows, 20.1.1–20.1.6.

Ha Minh, H., Viegas, J.R., Rubesin, M.W., Vendrome, D.D., Spalart, P., 1989. Physical analysis and second-order modelling of an unsteady turbulent flow: The oscillating boundary layer on a flat plate. Proc. 7th Symp. Turbulent Shear Flows, 11.5.1–11.5.6.

Inaoka, K., Matsui, M., Suzuki, K., 1997. Flow and heat transfer characteristics of a turbulent boundary layer disturbed by a square rod (Control of vortex shedding by means of a splitter plate). In: Hanjalic, K., Peters, T.W.J. (Eds.), Proc. of the 2nd Int. Symp. on Turbulence, Heat and Mass Transfer. Delft University Press, Delft, pp. 95–104.

Inaoka, K., Yamamoto, J., Suzuki, K., 1998. Heat transfer characteristics of a flat plate laminar boundary layer disturbed by a square rod. In: Proc. of 5th Int. Conf. on Advanced Comp. Methods in Heat Transfer, pp. 297–306.

Kato, M., Launder, B.E., 1993. The modelling of turbulent flow around stationary and vibrating square cylinders. Proc. 9th Symp. Turbulent Shear Flows, 10.4.1–10.4.6.

Kawaguchi, Y., Matsumori, Y., Suzuki, K., 1984. Structural study of momentum and heat transfer in the wall region of a disturbed turbulent boundary layer. Proc. 9th Biennial Symp. Turbulence, 28.1–28.10.

Launder, B.E., Sharma, B.I., 1974. Lett. Heat Mass Transfer 1, 131–138.

MacInnes, J.M., Claus, R.W., Huang, P.G., 1989. Time-dependent calculation of a forced mixing layer using a $k-\varepsilon$ turbulence model. Proc. 7th Symp. Turbulent Shear Flows, 11.4.1–11.4.6.

Mansour, N.N., Kim, J., Moin, P., 1988. Reynolds-stress dissipation-rate budgets in a turbulent channel flow. J. Fluid Mech. 194, 14–44.

Reynolds, W.C., Hussain, A.K.M.F., 1972. The mechanics of an organized wave in turbulent shear flow, Part 3: Theoretical models and comparisons with experiments. J. Fluid Mech. 54 (2), 263–288.

Suzuki, H., Suzuki, K., Sato, T., 1988. Dissimilarity between heat and mass transfer in a turbulent boundary layer disturbed by a cylinder. Int. J. Heat Mass Transfer 31 (2), 259–265.

Suzuki, K., Suzuki, H., Kikkawa, Y., Kigawa, H., Kawaguchi, Y., 1991. Heat transfer and skin friction of a flat plate turbulent boundary layer disturbed by a cylinder – The effect of cylinder diameter and clearance between the cylinder and the flat plate. Durst et al., F. (Eds.), Turbulent Shear Flows 7, 119–135.

Suzuki, K., Suzuki, H., 1994a. Unsteady heat transfer in a channel obstructed by an immersed body. Annual Review of Heat Transfer, vol. 5. Begell House Inc., 177–206.

Suzuki, K., Suzuki, H., 1994b. Instantaneous structure and statistical feature of unsteady flow in a channel obstructed by a square rod. Int. J. Heat Fluid Flow 15 (6), 426–437.

Suzuki, K., Xi, G.N., Inaoka, K., Hagiwara, Y., 1994. Mechanism of heat transfer enhancement due to self-sustained oscillation for an in-line fin array. Int. J. Heat Mass Transfer 37 (1), 83–96.

Suzuki, K., Inaoka, K., 1998. Flow modification and heat transfer enhancement with vortices. Int. J. Transport Phenomena 1, 17–30.

Yao M., Nakatani, M., Okuda, M., Suzuki, K., 1995. Wavelet analysis of the velocity and temperature signals measured in a channel obstructed by a square rod. Proc. 10th Symp. Turbulent Shear Flows, vol. 3, 28.19–28.24.